Multi-Nuclear Rare-Earth-Implanted Tartaric Acid-Functionalized Selenotungstates and Their Fluorescent and Magnetic Properties

Jinglin Liu, Dan Wang,* Xin Xu, Hailou Li, Junwei Zhao,* and Lijuan Chen*

| Read Online

ACCESS | Metrics & More | Article Recommendations | SI Supporting Information

ABSTRACT: A family of multinuclear rare-earth (RE)-implanted H_2tart^{2-}-functionalized selenotungstates (STs) $[H_2N(CH_3)_2]_{13}H\{[W_2O_5(OH)_2(H_2tart)_2](H_2tart)\{[W_3O_6RE_2(H_2O)_6][SeW_9O_{33}]_2\}_2\}\cdot 31H_2O$ [RE = Eu^{3+} (**1**), Tb^{3+} (**2**), Dy^{3+} (**3**), Ho^{3+} (**4**), Y^{3+} (**5**); H_4tart = D-tartaric acid] have been afforded by a simple one-pot aqueous reaction and were structurally characterized. Intriguingly, their isomorphous organic−inorganic hybrid anion $\{[W_2O_5(OH)_2(H_2tart)_2](H_2tart)\{[W_3O_6RE_2(H_2O)_6][SeW_9O_{33}]_2\}_2\}^{14-}$ includes two sandwich-type $\{[W_3O_6[RE_2(H_2O)_6][SeW_9O_{33}]_2\}^{4-}$ dimeric units with a W−O−RE heterometal core, which are further joined by two H_2tart^{2-}-decorated dinuclear tungsten-oxo $\{W_2O_5(OH)_2(H_2tart)_2\}$ clusters and a bridging H_2tart^{2-} ligand, contributing to a surprising Mobius band-like configuration. It is worth emphasizing that three H_2tart^{2-} ligands coordinate with tungsten centers rather than RE cations. For all we know, **1**−**5** delegate the infrequent RE-implanted STs functionalized by triplicate H_2tart^{2-} bridges. Furthermore, fluorescent performances of **1**−**4** as well as magnetic properties of **2**−**4** have been surveyed. The solid-state fluorescence emission spectra prove that each of them undoubtedly shows the characteristic emission peaks of RE cores, while alternating-current susceptibility measurements suggest field-induced single-molecule magnetic behavior in **3**.
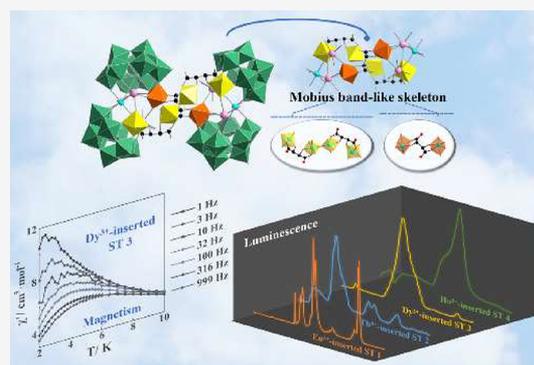
■ INTRODUCTION

Polyoxometalates (POMs) display abundant structural features, intriguing properties, and underlying applications in catalytic, magnetic, pharmic, optical, and nanotechnological aspects.[1−6] Polyoxotungstates (POTs), as an outstanding branch of POMs, are commonly employed as functional inorganic pluridentate oxygen-rich nominees to integrate oxyphilic d- or f-block metals for constructing TM- or RE-implanted POTs on the basis of highly electronegative and oxygen-rich surfaces.[7−10] Hitherto, a tremendous amount of RE-implanted POTs (REIPOTs) have been identified since Peacock and Weakley successfully obtained a class of REIPOTs $[RE(W_5O_{18})_2]^{n-}$ in 1971 and concurrently studied the reaction activities between RE ions and monovacant $[XW_{11}O_{39}]^{n-}$ (X = Si^{IV}, P^V)/$[P_2W_{17}O_{61}]^{10-}$ precursors to prepare 1:1- or 1:2-type Keggin or Dawson REIPOTs.[11−14] A great number of studies have afforded favorable evidence that the introduction of RE ions into the POT system matters a lot in POT chemistry. Other than endowing REIPOTs with considerable optical and magnetic behaviors, RE ions can further act as bridges to join tungsten−oxo segments together to give access to giant POT clusters owing to variable coordination configurations and large ionic radii of RE ions. A brand new world of RE-implanted selenotungstates (REISTs) was opened by the first two high-nuclear octameric REISTs by Su and co-workers in 2013,[15] followed by the acquirement of two Keggin and Dawson mixed REISTs in the next year.[16] As

is well known, ST clusters prefer to form various vacant structural units, benefiting from the effect of lone pair of electrons, and the naked vacant sites benefit to bind RE ions, which potentially results in a mass of novel and unique structures. Thereafter, REISTs have attracted the close attention of inorganic chemists in the past decade, and some prominent findings have been presented. Typically, our group has addressed two kinds of organocation and pH-controlled deca-RE embedded octameric ST aggregates (2017),[17] several Se^{IV} and RE simultaneously bridging REIPOTs constructed from vacant Dawson POT segments (2018 and 2019),[18,19] two Ce^{3+}-encapsulated STs (2019)[20] along with unprecedented RE-embedded STs containing mixed (P^{III}, Se^{IV})-heteroatom-oriented building blocks (2020).[21] What is noticeable is that such REISTs can be acquired by the one-step reaction of commercial chemicals, which manifest the huge potential of synergistic reactions of tungstate, selenite, and RE salts to create novel REISTs.
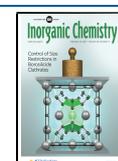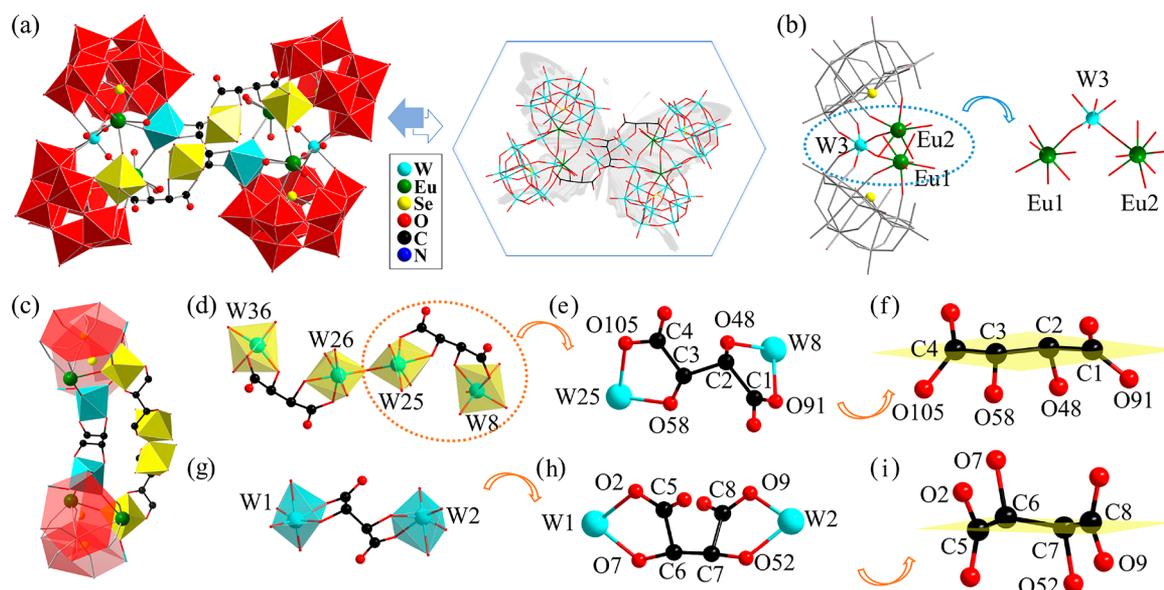
Figure 1. (a) Tetrameric **1a** anion. (b) The sandwich-type **1b** moiety. (c) Drawing of two H_2tart^{2-}-involving linkages connecting two **1b** moieties (some terminal oxygen atoms are abolished). (d) View of the $\{W_4O_9(OH)_2(H_2tart)_2\}$ segment. (e) Connection mode of the H_2tart^{2-} ligand bridging W8 and W25 atoms in $\{W_4O_9(OH)_2(H_2tart)_2\}$. (f) Side view of a H_2tart^{2-} ligand in $\{W_4O_9(OH)_2(H_2tart)_2\}$. (g) View of the $\{W_2O_4(H_2tart)\}$ segment. (h) Connection mode of the H_2tart^{2-} ligand bridging W1 and W2 atoms in $\{W_2O_4(H_2tart)\}$. (i) Side view of the H_2tart^{2-} ligand in $\{W_2O_4(H_2tart)\}$.

Recently, the pursuit of novel inorganic−organic hybrid REISTs (IOHREISTs) by continuously introducing RE cations and organic functional ligands into the ST system has appealed to researchers due to REISTs' outstanding latent applications in catalytic, magnetic, and photoelectric fields.[20−23] Even though much effort has been devoted to this research, only a few examples of IOHREISTs have been reported. Representatively, a case of glycine-modified tripraseodymium-implanted ST was obtained by Niu et al. in 2017.[22] Moreover, acetate-modified cerium-encapsulated STs have been obtained by our group, which can function as candidates for electrochemical detection of dopamine and paracetamol.[24] Nevertheless, the flexible H_4tart with two hydroxyl groups and two terminal carboxyl groups has not been reported in the construction of IOHREISTs, even though there are four potential coordination sites in its structure.

On this basis, H_4tart has been chosen in our system to modify REISTs, and as expected, for the first time, a family of triple-H_2tart^{2-} bridging REISTs $[H_2N(CH_3)_2]_{13}H\{[W_2O_5(OH)_2(H_2tart)_2](H_2tart)\{[W_3O_6RE_2(H_2O)_6][SeW_9O_{33}]_2\}_2\}\cdot31H_2O$ [RE = Eu^{3+} (**1**), Tb^{3+} (**2**), Dy^{3+} (**3**), Ho^{3+} (**4**), Y^{3+} (**5**)] have been harvested, representing fresh IOHREISTs with tartaric acid connectors. Unprecedentedly, the two terminal carboxyl groups and the middle hydroxyl groups in the H_4tart ligand coordinate with tungsten atoms rather than RE ions, serving as unique bridges which join four $[\alpha\text{-}SeW_9O_{33}]^{8-}$ ($\{SeW_9\}$) moieties. More intriguingly, the H_2tart^{2-}-jointing $\{[W_2O_5(OH)_2(H2tart)_2](H_2tart)\{[W_3O_6Eu_2(H_2O)_6]\}_2\}^{18-}$ fragment presents a rare Mobius ring configuration. Luminescent (LS) performances of **1**−**4** were investigated, demonstrating that their LS properties principally result from the featured emissions (EMs) of RE ions. Especially, the thermal stability of **3** was probed by poikilothermic LS measurements. At the same time, the field-induced single-molecule magnet (SMM) behavior of **3** was demonstrated via dynamic magnetic exploration. Moreover, magnetic properties of **2** and **4** were also studied in the range

of 1.8−300 K. This work not only offers enriched structural diversities of IOHREISTs but also expands the development potential of the one-step self-assembly approach of simple raw materials in synthetic chemistry of POM-based functional materials. More importantly, the structural modulation of the ST system by incorporating RE centers and carboxylic acid ligands has led to the purposeful design and synthesis of IOHREIST materials, providing data accumulation for the applications of REIPOT materials in fluorescence and magnetic fields.

■ RESULTS AND DISCUSSION

Structure Description. A summary of crystallographic parameters for **1**−**5** is given in Table S1. The chemical valences of W(+VI), RE(+III), and Se(+IV) elements in **1**−**5** are proved by bond-valence sum (BVS) calculations (Table S2).[25] Both infrared spectroscopy (IR) data (Figure S1) and powder X-ray diffraction (PXRD) patterns (Figure S2) qualify the isomorphic structures and good purity of **1**−**5**. **1**−**5** belong to the orthorhombic space group $P2_12_12_1$. Assisted by thermogravimetric analysis (Figure S3) and elemental analyses, the molecular formulas of **1**−**5** are determined as $[H_2N(CH_3)_2]_{13}H\{[W_2O_5(OH)_2(H_2tart)_2](H_2tart)\{[W_3O_6RE_2(H_2O)_6][SeW_9O_{33}]_2\}_2\}\cdot31H_2O$ [RE = Eu^{3+} (**1**), Tb^{3+} (**2**), Dy^{3+} (**3**), Ho^{3+} (**4**), Y^{3+} (**5**)], consisting of an inorganic−organic hybrid butterfly-shaped $\{[W_2O_5(OH)_2(H_2tart)_2](H_2tart)\{[W_3O_6RE_2(H_2O)_6][SeW_9O_{33}]_2\}_2\}^{14-}$ anion, thirteen $[H_2N(CH_3)_2]^+$ cations, one H^+ cation, and thirty-one lattice waters. Therefore, **1** is selected as an example to elaborate the crystal structure. The centric butterfly-shaped $\{[W_2O_5(OH)_2(H_2tart)_2](H_2tart)\{[W_3O_6Eu_2(H_2O)_6][SeW_9O_{33}]_2\}_2\}^{14-}$ (**1a**) anion (Figure 1a) can be described as the combination of two sandwich-type $[Eu_2(H_2O)_6WO_2(\alpha\text{-}SeW_9O_{33})_2]^{16-}$ (**1b**) dimeric moieties (Figure 1b) connected by two H_2tart^{2-}-involving linkages (Figure 1c), which are severally marked as $\{W_4O_9(OH)_2(H_2tart)_2\}$ (Figure 1d) and $\{W_2O_4(H_2tart)\}$

(Figure 1g). Each **1b** moiety is composed of two trivacant $\{SeW_9\}$ fragments sandwiched by a trimetal $\{Eu_2W\}$ unit through bridging oxygen atoms, resulting in a triangular configuration (Figure 1b). Intriguingly, three H_2tart^{2-} ligands show different torsion modes. In the $\{W_4(H_2tart)_2\}$ moiety, each of two tartaric acid linkers connects two W atoms to form a long chain structure with a length of 12.824 Å (Figure 1d). Furthermore, four carbon atoms present a zigzag fashion with two hydroxy groups on the opposite sides of the chain (Figure 1e, f), marked as coordination mode A. On the other hand, a slightly twisted U-type configuration is observed in the $\{W_2(H_2tart)\}$ (Figure 1e), while two −OH groups respectively lie above and below the C5−C6−C7−C8 plane (Figure 1h, i), denoted as coordination mode B. The chain length of the $\{W_2(H_2tart)\}$ cluster is about 6.6727 Å, which is nearly the half length of the longer $\{W_4(H_2tart)_2\}$ chain. Moreover, every pair of adjacent oxhydryl and carboxyl groups in each H_2tart^{2-} chelate one W^{VI} atom, thus bridging discrete tungsten−oxo clusters together through six C−O−W−O−C rings constructing the fabulous crystal skeleton. Four eight-coordinated Eu^{3+} nuclei all live in the contorted bicapped trigonal prism with Eu−O distances of 2.289(19)−2.51(2) Å (Figure S4). Another highlight in **1a** is that after removing four $\{SeW_9\}$ units, the central $\{[W_2O_5(OH)_2(H_2tart)_2](H_2tart)-\{[W_3O_6Eu_2(H_2O)_6]\}_2\}^{18-}$ (**1c**, Figure 2a) moiety reveals a
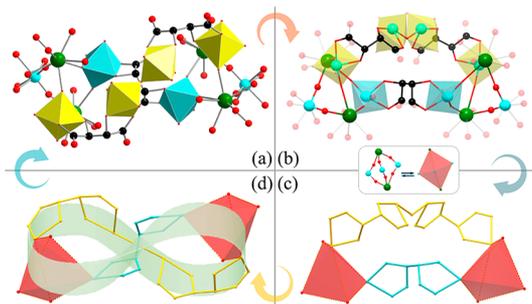

Figure 2. (a) Central **1c** fragment. (b) Cricoid framework constructed by H_2tart^{2-} bridging W atoms and Eu ions. (c) Simplified graph of **1c**. (d) Schematic representation of the Mobius band-like skeleton.

Mobius band-like appearance, which can be clearly observed from the simplified graph, while the $\{Eu_2W_3\}$ segment presents a trigonal bipyramid construction (Figure 2b, c). To be specific, one H_2tart^{2-} ligand and one organic−inorganic hybrid $[W_2O_5(OH)_2(H2tart)_2]^{14-}$ cluster collectively bridge two $\{Eu_2W_3\}$ moieties by jointing apical W atoms. An approximate Mobius strip configuration unfolds (Figure 2d), and as far as we know, no similar structure has ever been reported, even though tartaric acid decorated POTs have been obtained previously. For details, Xu et al. achieved two enantiomerically Ce^{III}-substituted silicotungstates decorated with tartaric acids (D-/L-SiW; Figure 3a) in 2014.[26] A pentagonal chelating ring (C−O−W−O−C) is observed while the other carboxylic O atom connects the Ce^{III} ion and the second hydroxy O atom coordinates with a W atom. Interestingly, the carboxyl group on the other end is naked. Whereafter, Niu's group synthesized a series of quadruple-tartaric acid bridging polytungstoarsenates (QT-AsW, 2015) and double-tartaric linking phospho-tungstates (DT-PW, 2016).[27,28] As reported, two of four tartaric acids in QT-AsW chelate two RE ions while two other ligands hold four RE ions (Figure 3b). In addition, two H_4tart
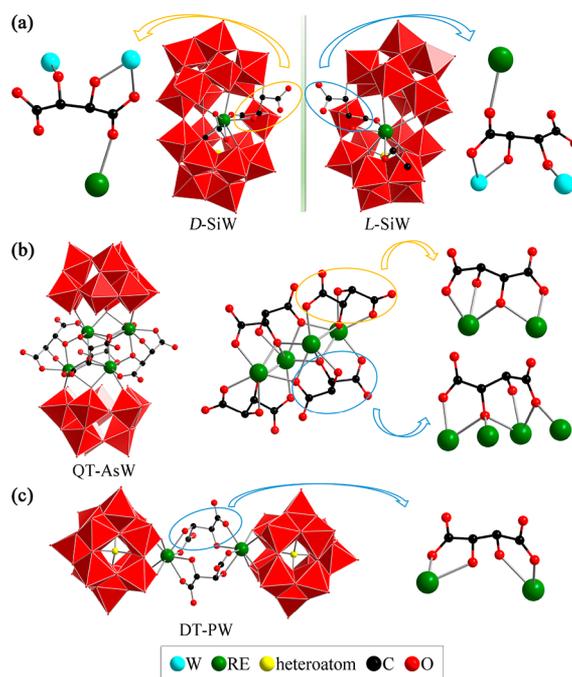

Figure 3. (a) The two enantiomerically Ce^{III}-substituted silicotung-states. (b) The quadruple-tartaric acid bridging polytungstoarsenate. (c) The double-tartaric linking phosphotungstate.

molecules bridge two RE-substituted $[RE(\alpha\text{-}PW_{11}O_{39})]^{4-}$ moieties in the DT-PW (Figure 3c).[29] As we can see from the above information, the coordination modes of tartaric acids in all other reported works are similar to coordination mode A in **1**, which further indicates the specificity of the B coordination mode of H_4tart in our compounds.

The counter cations (H^+ and $[H_2N(CH_3)_2]^+$) and lattice waters are omitted so that the stacking mode of **1a** anions can be better understood. Specifically, every **1a** anion can be simplified as a parallelogram using Se^{IV} vertexes along each direction (Figure S5a−c). Obviously, the alignment of **1a** anions exhibits the −AAA− motif along every axial direction (Figure S5d−f), which could be explicitly observed from the simplified diagrams (Figure S5g−i). Noteworthily, inserting RE ions to POMs has become a crucial domain in supramolecular chemistry, in which the resulting RE-inserted POM units are able to be interacted with by H-bonding or van der Waals interactions. So, the generated three-dimensional supramolecular frameworks may be considered as promising candidates for use in chemical biology, materials chemistry, etc.[30−32] H-bonding interactions between nitrogen atoms of H_2tart^{2-} ligands and between oxygen atoms of ST subunits and water molecules lead to a three-dimensional supramolecular structure of **1** with N−H···O distances of 2.97(4)−3.21(4) Å and O−H···O distances of 2.89(4)−3.27(4) Å.

LS Properties. As we all know, RE-based complexes have evoked huge interests in biomedical analyses, light-emitting diodes, cathode ray tubes, and light conversion devices because of peculiar LS characteristics of RE ions (narrow EM bandwidth, long EM lifetime, and large Stokes shift), which stem from electron transitions inside the 4f shell of RE ions along with the shielding effect of the closed $5s^2$ and $5p^6$ shells on the partially filled 4f orbits.[33] In this work, solid-state LS properties of **1**−**4** were researched at ambient temperature.

Upon excitation of 394 nm, the EM spectrogram (EMS) of **1** was collected, which exhibits eight typical EM peaks of Eu^{3+} ions, namely, 526, 537, 554, 580, 593, 615, 651, and 702 nm, being separately affiliated to $^5D_1 \rightarrow {}^7F_0$, $^5D_1 \rightarrow {}^7F_1$, $^5D_1 \rightarrow {}^7F_2$, $^5D_0 \rightarrow {}^7F_0$, $^5D_0 \rightarrow {}^7F_1$, $^5D_0 \rightarrow {}^7F_2$, $^5D_0 \rightarrow {}^7F_3$, and $^5D_0 \rightarrow {}^7F_4$ transitions (Figure S6a).[34] At the same time, the excitation spectrogram (EXS) of **1** (λ_{em} = 615 nm) comprises five signal peaks, where the strongest signal peak at 394 nm corresponds to the $^7F_0 \rightarrow {}^5L_6$ transition in Eu^{3+} ions, while the other five weak peaks at 362, 376, 394, 417, and 465 nm are separately identified as $^7F_0 \rightarrow {}^5D_4$, $^7F_0 \rightarrow {}^5G_2$, $^7F_0 \rightarrow {}^5L_6$, $^7F_0 \rightarrow {}^5D_3$, and $^7F_0 \rightarrow {}^5D_2$ transitions (Figure S6b).[35] Because the $^5D_0 \rightarrow {}^7F_0$ EM is symmetry forbidden in the symmetrical surroundings, its emergence at 580 nm in EMS of **1** implies that Eu^{3+} ions are located in low-symmetry environment, coinciding with the twisted bicapped trigonal prisms of Eu^{3+} ions. In general, the $^5D_0 \rightarrow {}^7F_{1,3}$ EMs are insensitive to the local ligand surroundings, and the $^5D_0 \rightarrow {}^7F_1$ EM intensity (EMI) varies very sightly with the ligand-field variation of Eu^{3+} ions.[34] On the contrary, the $^5D_0 \rightarrow {}^7F_{0,2,4}$ EMs are very susceptive to the local ligand surroundings so that the $^5D_0 \rightarrow {}^7F_2$ EMI highly depends on the local symmetry of Eu^{3+} ions.[35] Hence, the local symmetry of Eu^{3+} ions can be evaluated by the $I_1(^5D_0 \rightarrow {}^7F_2)/I_2(^5D_0 \rightarrow {}^7F_1)$ EMI ratio. For **1**, the EMI ratio of ca. 2.38 reflects lower symmetrical surroundings of Eu^{3+} ions. By monitoring the strongest $^5D_0 \rightarrow {}^7F_2$ EM, the obtained LS decay profile (LSDP) of **1** (Figure S6c) can be well conformed to the monoexponential function, providing a lifetime of 286.78 μs (100%) and preexponential factor of 3271.39. In addition, the red-light EM of **1** was determined by the corresponding LS spectrum as (0.55586, 0.36632) in the CIE chromaticity coordinates (Figure S7). In addition, variable-temperature EMSs of **1** in the 500−750 nm range were measured when the temperature was varied from 80 to 300 K (Figure 4). As can be clearly seen from Figure 4, the EMI of **1**
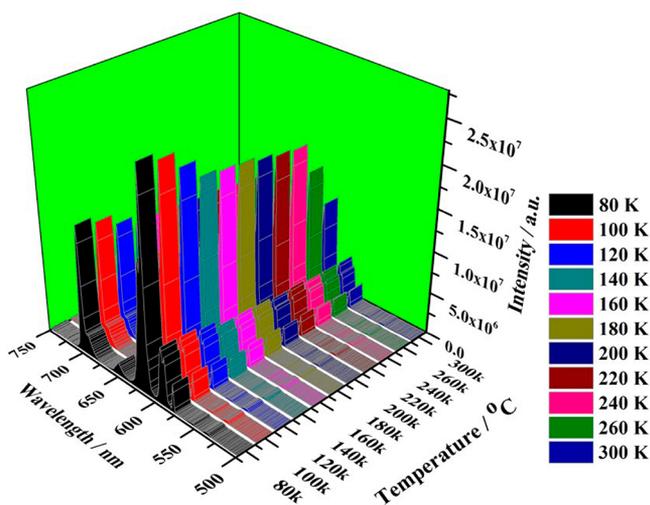

Figure 4. Variable-temperature EMSs of **1** in 500−750 nm.

slowly declines as the temperature increases from 80 to 240 K on account of the thermal quenching effect.[36] To be specific, as the temperature rises, the velocity of the molecules is accelerated, the probability of intermolecular vibration is increased, and the nonradiative transition and deactivation are increased, thus reducing the FL emission intensity. Of concern is that the decrease of the EMI of **1** becomes rapid upon the

temperature being higher than 260 K, which can be assigned to the starting change of **1a** that can be proved by thermogravimetric analysis result (Figure S3).

In a similar way, the LS performances of **2**, **3**, and **4** have also been explored and the typical LS behaviors of corresponding RE ions are observed as expected, while **5** has no RE-centered EM because of the empty 4f shell in the Y^{3+} ion. In detail, **2** emits green emission (λ_{ex} = 378 nm) and displays four prominent EM peaks at 495 ($^5D_4 \rightarrow {}^7F_6$), 544 ($^5D_4 \rightarrow {}^7F_5$), 582 ($^5D_4 \rightarrow {}^7F_4$), and 622 ($^5D_4 \rightarrow {}^7F_3$) nm and three feeble EM peaks at 647 ($^5D_4 \rightarrow {}^7F_2$), 670 ($^5D_4 \rightarrow {}^7F_1$), and 679 ($^5D_4 \rightarrow {}^7F_0$) nm (Figure 5a).[37] Furthermore, by observing the strongest EM at 544 nm, the EXS of **2** shows three bands at 358 ($^7F_6 \rightarrow {}^5L_6$), 369 ($^7F_6 \rightarrow {}^5L_9$), and 378 ($^7F_6 \rightarrow {}^5G_6$) nm.[38] In addition, for **2**, the LSDP (λ_{em} = 544 nm) can be matched by the biexponential function $I = A_1 \exp(-t/\tau_1) + A_2 \exp(-t/\tau_2)$ (where τ_1 and τ_2 are the fast and slow components of the lifetimes, respectively, and A_1 and A_2 are the corresponding pre-exponential divisors, respectively). Theoretically, the fitting lifetimes are τ_1 = 57.72 μs (25.94%) and τ_2 = 141.57 μs (74.06%), while the pre-exponential divisors are A_1 = 662.66 and A_2 = 771.27. The average decay time (τ^*) can be calculated as 119.82 μs by the expression $\tau^* = (A_1\tau_1^2 + A_2\tau_2^2)/(A_1\tau_1 + A_2\tau_2)$ (Figure 5b).[39] The EMS of **3** (λ_{ex} = 388 nm) demonstrates the characteristic EM of Dy^{3+} ions originating from the intra-4f^{10} $^4F_{9/2} \rightarrow {}^6H_J$ (J = 15/2, 13/2, and 11/2) (Figure 5c).[40] The EM peaks at 489 and 663 nm are ascribed to $^4F_{9/2} \rightarrow {}^6H_{15/2}$ and $^4F_{9/2} \rightarrow {}^6H_{11/2}$ transitions, while the most conspicuous EM peak at 573 nm roots in the highly sensitive $^4F_{9/2} \rightarrow {}^6H_{13/2}$ transition strongly affected by the Dy^{3+} local circumstances.[41,42] The LSDP of **3** was also collected by observing the 573 nm EM (Figure 5d), which obeys the biexponential function, generating the average lifetime (τ^*) of 6.09 μs with τ_1 = 3.25 μs (56.76%) and τ_2 = 9.81 μs (43.24%). In the case of **4**, its EMS under the 452 nm EX shows the Ho^{3+} LS bands resulting from $(^5S_2)^5F_4 \rightarrow {}^5I_8$ (529 nm) and $^5F_5 \rightarrow {}^5I_6$ (658 nm) transitions (Figure 5e), and its LSDP gives out a τ^* value of 7.71 μs (Figure 5f). The CIE color coordinates of **1**−**4** can be explicitly seen (Figure S7).

Magnetic Properties. During the last few decades, a tremendous advancement in the magnetism study of RE-containing complexes has been witnessed benefiting from intrinsic anisotropy and particular electron configurations. Peculiarly, the magnetic natural instincts for Eu^{3+} and Sm^{3+} ions are markedly disparate. The small energy-level difference between the ground state and first excited state for Eu^{3+} (400 cm^{-1}) and Sm^{3+} (1000 cm^{-1}) may often lead to thermal population of the first excited state at room temperature; therefore, the thermal population of the higher energy state and crystal field effect should be considered for Eu^{3+}- and Sm^{3+}-inserted complexes.[43] Upon lowing temperature, thermal depopulation of the Stark sublevels can result in the change of the magnetic moment of RE ions, which makes magnetic susceptibilities diverge from Curie behavior.[44] In this work, magnetic properties of **2**, **3**, and **4** were tested in an external field of 1000 Oe at 1.8−300 K (Figure 6). The $\chi_m T$ of **2** (χ_m is the molar magnetic susceptibility and T is temperature) is shown in Figure 6a. Obviously, the $\chi_m T$ at 300 K (58.74 emu^3 K mol^{-1}) is somewhat higher than the theoretical value of four uncoupled Tb^{3+} (47.27 emu^3 K mol^{-1}). As temperature decreases, the $\chi_m T$ also gradually decreases until it reaches 42.41 emu^3 K mol^{-1} at 1.8 K, which might be connected with the orbital coupling of Tb^{3+} ions and the depopulation effect of
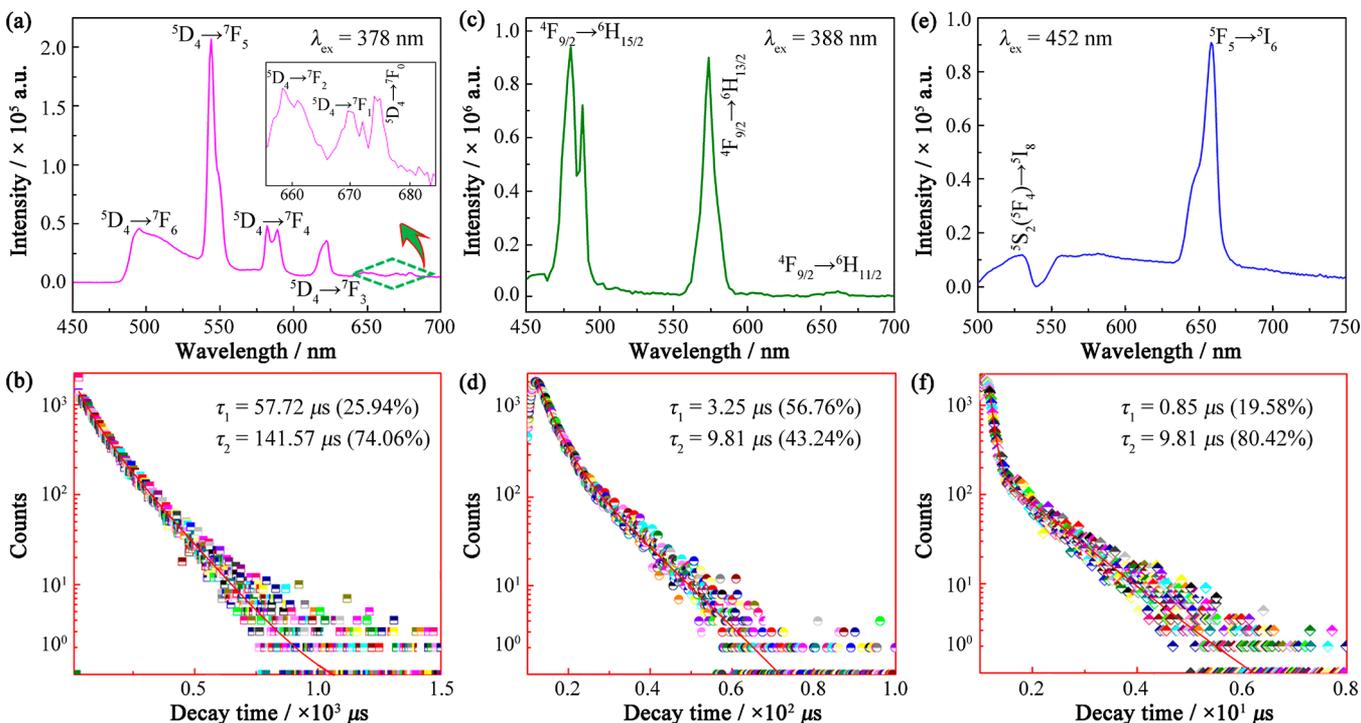
Figure 5. (a) EMS of **2** upon the 378 nm EX. (b) LSDP of **2** taken by observing the 544 nm EM. (c) EMS of **3** upon the 388 nm EX. (d) LSDP of **3** taken by observing the 573 nm EM. (e) EMS of **4** upon the 452 nm EX. (f) LSDP of **4** taken by observing the 658 nm EM.
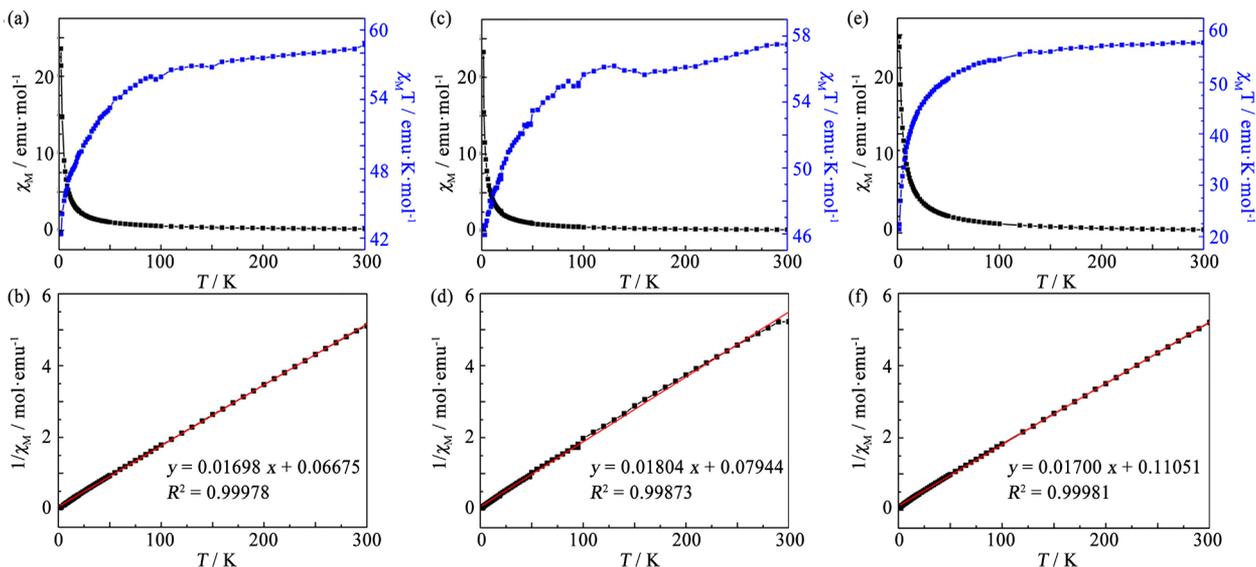

Figure 6. (a) Temperature-dependent curves of χ_m and χ_mT for **2** at 1.8−300 K. (b) The plot of $1/\chi_m$ and T for **2**. (c) Temperature-dependent curves of χ_m and χ_mT for **3** at 1.8−300 K. (d) The plot of $1/\chi_m$ and T for **3**. (e) Temperature-dependent curves of χ_m and χ_mT for **4** at 1.8−300 K. (f) The plot of $1/\chi_m$ and T for **4**. The red solid lines in (b), (d), and (f) represent the best-fit results by the Curie−Weiss law.

excited state electrons induced by the ligand field effect. Besides this, the plot of $1/\chi_m$ versus T of **2** conforms to the Curie−Weiss law (1.8−300 K; Figure 6b), offering a Curie constant (C) of 58.89 cm^3 K mol^{-1} and a Weiss constant (θ) of −3.93 K, with the correlation coefficient R^2 of 0.9998. This small negative Weiss value indicates a weak antiferromagnetic (AFM) interaction and the depopulation effect of excited-state electrons of Tb^{3+} ions. For **3**, its temperature-varying magnetic susceptibility curve is very similar to that of **2**, and the χ_mT at room temperature (57.48 emu^3 K mol^{-1}) is in close proximity to the calculated value (56.68 emu^3 K mol^{-1}) for four

independent Dy^{3+} ions ($S = 5/2$, $L = 5$, $^6H_{15/2}$, $g = 4/3$).[45] The χ_mT decreases with decreasing temperature, and the value is found to be 46.65 emu^3 K mol^{-1} at 1.8 K, which results from the dedwelling action of the excited electrons and the weak AFM interaction of Dy^{3+} ions (Figure 6c). Furthermore, between 1.8 and 300 K, the plot of $1/\chi_m$ and T for **3** is also in accordance with Curie−Weiss law ($C = 55.43$ emu^3 K mol^{-1}, $\theta = -4.40$ K, $R^2 = 0.99873$; Figure 6d). For **4**, its χ_mT at 300 K is 57.74 emu^3 K mol^{-1}, which is close to the theoretical value of 56.28 emu^3 K mol^{-1} for four uncoupled Ho^{3+} ions ($S = 2$, $L = 6$, $g = 5/4$).[46,47] The χ_mT reduces to 21.38 emu^3 K mol^{-1} when
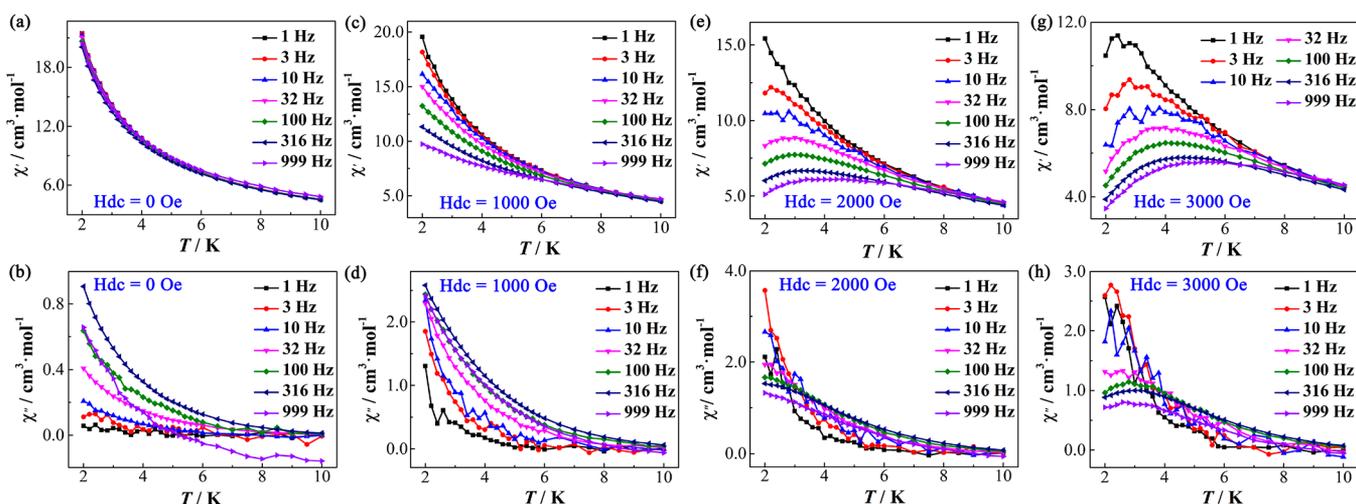
Figure 7. Ac susceptibility curves for **3** under different external magnetic fields of (a, b) 0 Oe; (c, d) 1000 Oe; (e, f) 2000 Oe; and (g, h) 3000 Oe.

the temperature is 1.8 K, which likely results from the dedwelling action of the excited electrons and the weak AFM interaction of Ho^{3+} ions (Figure 6e). Besides this, the relationship between $1/\chi_m$ and T (1.8–300 K) for **4** follows the Curie–Weiss law (C = 58.82 emu^3 K mol^{-1}, θ = −6.50 K, R^2 = 0.99981; Figure 6f).

More importantly, significant attention has been paid to the exploration of special magnetic behavior such as SMM due to underlying applications in information processing, data storage, and quantum computing.[48,49] As has been demonstrated, Dy^{3+} ions have large intrinsic magnetic anisotropy as well as a large energy gap and magnetic quantum number (m_J) between the ground state and the first excited state, making for a high energy barrier (U_{eff}) value for Dy^{3+}-based SMMs. Nevertheless, the greatest problem in developing SMMs is that increasing the spin ground state of a molecule is often at the expense of reducing the magnetic anisotropy of the system. Since 4f electrons in RE ions are shielded by 5s and 5p electrons, both the problem in strengthening the magnetic interaction intensity between RE ions and the generalized existence of the quantum tunneling effect (QTE) make it a challenging topic to enhance the magnetic anisotropy energy barrier for the development of RE-based SMMs. Therefore, we tested the ac susceptibility of **3** over 1.8 to 10 K without any applied magnetic field. As shown in Figure 7a and 7b, the real signal (χ') of **3** is substantially coincident while the imaginary signal (χ'') increases with enlarged frequency, and such a significant frequency dependence indicates a typical slow magnetic relaxation phenomenon and possible SMM behavior.[50] However, due to QTE in RE-based composites,[51,52] the maximum χ'' value does not appear within the temperature range and frequency range studied, preventing the determination of the barrier ($\Delta E/k_B$) and relaxation time (τ_0). To suppress the influence of the above-mentioned QTE, ac susceptibility tests under different magnetic fields (1000–3000 Oe) were conducted as well. Specifically, the frequency dependence of χ' and χ'' gradually increases as the magnetic field is increased, testifying to a suppressed QTE (Figure 7c–f). When the applied magnetic field reaches 3000 Oe, the imaginary part χ'' shows a clearly visible peak value while the ac frequency ranges from 1.00 to 999.04 Hz (Figure 7g, h), which indicates that **3** exhibits a field-induced SMM behavior.[53–55] Moreover, the peak value of around 4.5 K

(3000 Oe) can be possibly attributed to the large field-induced intermolecular interactions rather than to the molecule-originated coupling effect. Therefore, POMs with abundant active O sites, which can be further incorporated with using magnetic metal clusters, are becoming a hot topic in building advanced magnetic materials.[56,57]

CONCLUSIONS

A series of unprecedented H_2tart^{2-}-functionalized REISTs $[H_2N(CH_3)_2]_{13}H\{[W_2O_5(OH)_2(H_2tart)_2](H_2tart)-\{[W_3O_6RE_2(H_2O)_6][SeW_9O_{33}]_2\}_2\}\cdot31H_2O$ [RE = Eu^{3+} (**1**), Tb^{3+} (**2**), Dy^{3+} (**3**), Ho^{3+} (**4**), Y^{3+} (**5**)] have been creatively presented in this work, which comprise an isomorphic tetrameric lacunary Keggin-type anion $\{[W_2O_5(OH)_2(H_2tart)_2](H_2tart)\{[W_3O_6RE_2(H_2O)_6][SeW_9O_{33}]_2\}_2\}^{14-}$ built by two sandwich-type $\{[W_3O_6[RE_2(H_2O)_6][SeW_9O_{33}]_2\}^{4-}$ dimeric units and a H_2tart-bridged W−RE-heterometal core. It should be noted that a Mobius ring configuration of the H_2tart^{2-} jointing $\{[W_2O_5(OH)_2(H_2tart)_2](H_2tart)-\{[W_3O_6Eu_2(H_2O)_6]\}_2\}^{18-}$ segment appears, which is unprecedented thus far. Their LS and magnetic performances which benefit from unique electron configurations of RE ions have been studied. Particularly, the Dy^{3+}-embedded **3** exhibits distinctive field-induced SMM behavior in addition to its LS property, which potentially makes it a promising candidate in optical and magnetic fields. Future research on introducing additional types of flexible and/or rigid organic ligands into STs will be conducted, along with pursuing TM ions and RE ions co-embedded STs, which are expected to enrich the fresh world of the heterometallic ST chemistry and improve LS and magnetic performances of OIHREISTs.

ASSOCIATED CONTENT

ⓈI Supporting Information

The Supporting Information is available free of charge at https://pubs.acs.org/doi/10.1021/acs.inorgchem.0c03443.

Experimental section; IR, PXRD, TG, and related structural figures; luminescence and magnetic figures; and BVS calculations of W, Se, and RE atoms in **1−5** (PDF)

Accession Codes

■ AUTHOR INFORMATION

Corresponding Authors

Dan Wang − *Henan Key Laboratory of Polyoxometalate Chemistry, College of Chemistry and Chemical Engineering, Henan University, Kaifeng, Henan 475004, China;* Email: wangdan@henu.edu.cn

Junwei Zhao − *Henan Key Laboratory of Polyoxometalate Chemistry, College of Chemistry and Chemical Engineering, Henan University, Kaifeng, Henan 475004, China;* orcid.org/0000-0002-7685-1309; Email: zhaojunwei@henu.edu.cn

Lijuan Chen − *Henan Key Laboratory of Polyoxometalate Chemistry, College of Chemistry and Chemical Engineering, Henan University, Kaifeng, Henan 475004, China;* Email: ljchen@henu.edu.cn

Authors

Jinglin Liu − *Henan Key Laboratory of Polyoxometalate Chemistry, College of Chemistry and Chemical Engineering, Henan University, Kaifeng, Henan 475004, China*

Xin Xu − *Henan Key Laboratory of Polyoxometalate Chemistry, College of Chemistry and Chemical Engineering, Henan University, Kaifeng, Henan 475004, China*

Hailou Li − *Henan Key Laboratory of Polyoxometalate Chemistry, College of Chemistry and Chemical Engineering, Henan University, Kaifeng, Henan 475004, China*

Complete contact information is available at:
https://pubs.acs.org/10.1021/acs.inorgchem.0c03443

Notes

The authors declare no competing financial interest.

■ ACKNOWLEDGMENTS

■ REFERENCES

(1) Zhang, J. W.; Huang, Y. C.; Li, G.; Wei, Y. G. Recent advances in alkoxylation chemistry of polyoxometalates: From synthetic strategies, structural overviews to functional applications. *Coord. Chem. Rev.* **2019**, *378*, 395−414.

(2) Dong, J.; Hu, J. F.; Chi, Y. N.; Lin, Z. G.; Zou, B.; Yang, S.; Hill, C. L.; Hu, C. W. A polyoxoniobate-polyoxovanadate double-anion catalyst for simultaneous oxidative and hydrolytic decontamination of chemical warfare agent simulants. *Angew. Chem., Int. Ed.* **2017**, *56*, 4473−4477.

(3) Ma, P. T.; Hu, F.; Wang, J. P.; Niu, J. Y. Carboxylate covalently modified polyoxometalates: From synthesis, structural diversity to applications. *Coord. Chem. Rev.* **2019**, *378*, 281−309.

(4) Wang, Z.; Liu, J. W.; Su, H. F.; Zhao, Q. Q.; Kurmoo, M.; Wang, X. P.; Tung, C. H.; Sun, D.; Zheng, L. S. Chalcogens-induced

Ag(6)Z(4)@Ag-36 (Z = S or Se) core-shell nanoclusters: enlarged tetrahedral core and homochiral crystallization. *J. Am. Chem. Soc.* **2019**, *141*, 17884−17890.

(5) Miras, H. N.; Richmond, C. J.; Long, D.-L.; Cronin, L. Solution phase monitoring of the structural evolution of a molybdenum blue nanoring. *J. Am. Chem. Soc.* **2012**, *134*, 3816−3824.

(6) Song, Y.-F.; Tsunashima, R. Recent advances on polyoxometalate based molecular and composite materials. *Chem. Soc. Rev.* **2012**, *41*, 7384−7402.

(7) Li, X. X.; Zhao, D.; Zheng, S. T. Recent advances in POM-organic frameworks and POM-organic polyhedra. *Coord. Chem. Rev.* **2019**, *397*, 220−240.

(8) Haider, A.; Bassil, B. S.; Soriano-Lopez, J.; Qasim, H. M.; Sáenz de Pipaón, C.; Ibrahim, M.; Dutta, D.; Koo, Y. S.; Carbo, J. J.; Poblet, J. M.; Galan-Mascaros, J. R.; Kortz, U. 9-Cobalt(II)-Containing 27-Tungsto-3-germanate(IV): Synthesis, Structure, Computational Modeling, and Heterogeneous Water Oxidation Catalysis. *Inorg. Chem.* **2019**, *58*, 11308−11316.

(9) Zhao, J.-W.; Li, Y.-Z.; Chen, L.-J.; Yang, G.-Y. Research progress on polyoxometalate-based transition-metal−rare-earth heterometallic derived materials: synthetic strategies. *Chem. Commun.* **2016**, *52*, 4418−4445.

(10) Huang, L.; Wang, S.-S.; Zhao, J.-W.; Cheng, L.; Yang, G.-Y. Synergistic combination of multi-Zr^{IV} cations and lacunary Keggin germanotungstates leading to a gigantic Zr$_{24}$-cluster-substituted polyoxometalate. *J. Am. Chem. Soc.* **2014**, *136*, 7637−7642.

(11) Peacock, R. D.; Weakley, T. J. R. Heteropolytungstate complexes of the lanthanide elements. Part I. preparation and reactions. *J. Chem. Soc. A* **1971**, 1836−1839.

(12) Peacock, R. D.; Weakley, T. J. R. Heteropolytungstate complexes of the lanthanide elements. Part II. electronic spectra: a metal-ligand charge-transfer transition of cerium(III). *J. Chem. Soc. A* **1971**, *0*, 1937−1940.

(13) Ma, X.; Yang, W.; Chen, L. J.; Zhao, J. W. Significant developments on rare-earth-containing polyoxometalate chemistry: synthetic strategies, structural diversities and correlative properties. *CrystEngComm* **2015**, *17*, 8175−8197.

(14) Liu, J.-C.; Han, Q.; Chen, L.-J.; Zhao, J.-W.; Streb, C.; Song, Y.-F. Aggregation of giant cerium−bismuth tungstate clusters into a 3D porous framework with high proton conductivity. *Angew. Chem., Int. Ed.* **2018**, *57*, 8416−8420.

(15) Chen, W.-C.; Li, H.-L.; Wang, X.-L.; Shao, K.-Z.; Su, Z.-M.; Wang, E.-B. Assembly of cerium(III)-stabilized polyoxotungstate nanoclusters with SeO$_3^{2−}$/TeO$_3^{2−}$ templates: from single polyoxoanions to inorganic hollow spheres in dilute solution. *Chem. - Eur. J.* **2013**, *19*, 11007−11015.

(16) Chen, W. C.; Yan, L. K.; Wu, C. X.; Wang, X. L.; Shao, K. Z.; Su, Z. M.; Wang, E. B. Assembly of Keggin-/Dawson-type polyoxotungstate clusters with different metal units and SeO$_3^{2−}$ heteroanion templates. *Cryst. Growth Des.* **2014**, *14*, 5099−5110.

(17) Liu, Y. J.; Li, H. L.; Lu, C. T.; Gong, P. J.; Ma, X. Y.; Chen, L. J.; Zhao, J. W. Organocounterions-assisted and pH-controlled self-assembly of five nanoscale high-nuclear lanthanide substituted heteropolytungstates. *Cryst. Growth Des.* **2017**, *17*, 3917−4029.

(18) Li, H.-L.; Liu, Y.-J.; Li, Y.-M.; Chen, L.-J.; Zhao, J.-W.; Yang, G.-Y. Unprecedented selenium and lanthanide simultaneously bridging selenotungstate aggregates stabilized by four tetravacant Dawson-like {Se$_2$W$_{14}$} units. *Chem. - Asian J.* **2018**, *13*, 2897−2906.

(19) Zhang, Y.; Li, Y. M.; Pang, J. J.; Liu, Y. F.; Li, P.; Chen, L. J.; Zhao, J. W. Two penta-RE^{III} encapsulated tetravacant Dawson selenotungstates and nanoscale derivatives and their luminescence properties. *Inorg. Chem.* **2019**, *58*, 7078−7090.

(20) Li, H. L.; Liu, Y. J.; Li, Y. M.; Chen, L. J.; Zhao, J. W.; Yang, G. Y. Unprecedented selenium and lanthanide simultaneously bridging selenotungstate aggregates stabilized by four tetra-vacant Dawson-like {Se$_2$W$_{14}$} units. *Chem. - Asian J.* **2018**, *13*, 2897−2907.

(21) Liu, L. L.; Jiang, J.; Liu, X. Y.; Liu, G. P.; Wang, D.; Chen, L. J.; Zhao, J. W. First series of mixed (P^{III}, Se^{IV})-heteroatoms oriented

rare-earth embedded polyoxotungstates containing distinct building blocks. *Inorg. Chem. Front.* **2020**, *7*, 4640.

(22) Yang, L.; Li, L.; Guo, J. P.; Liu, Q. S.; Ma, P. T.; Niu, J. Y.; Wang, J. P. A nanosized Gly-decorated praseodymium-stabilized nanosized selenotungstate cluster: synthesis, structure, and oxidation catalysis. *Chem. - Asian J.* **2017**, *12*, 2441−2446.

(23) Zhang, Y.; Li, Y. J.; Pang, J. J.; Liu, Y. F.; Li, P.; Chen, L. J.; Zhao, J. W. Two penta-REIII encapsulated tetravacant dawson selenotungstates and nanoscale derivatives and their luminescence properties. *Inorg. Chem.* **2019**, *58*, 7078−7090.

(24) Jiang, J.; Liu, L. L.; Liu, G. P.; Wang, D.; Zhang, Y.; Chen, L. J.; Zhao, J. W. Organic-inorganic hybrid cerium-encapsulated seleno-tungstate including three building blocks and its electrochemical detection of dopamine and paracetamol. *Inorg. Chem.* **2020**, *59*, 15355−15364.

(25) Brown, I. D.; Altermatt, D. Bond-valence parameters obtained from a systematic analysis of the inorganic crystal structure database. *Acta Crystallogr., Sect. B: Struct. Sci.* **1985**, *B41*, 244−247.

(26) Ju, W.-W.; Zhang, H.-T.; Xu, X.; Zhang, Y.; Xu, Y. Enantiomerically pure lanthanide − organic polytungstates exhibiting two-photon absorption properties. *Inorg. Chem.* **2014**, *53*, 3269−3271.

(27) Wang, Y.; Sun, X. P.; Li, S. Z.; Ma, P. T.; Wang, J. P.; Niu, J. Y. Synthesis and magnetic properties of tartrate-bridging rare-earth-containing polytungstoarsenate aggregates from an adaptive precursor $[As_2W_{19}O_{67}(H_2O)]^{14−}$. *Dalton Trans.* **2015**, *44*, 733−738.

(28) Ma, P. T.; Wan, R.; Si, Y. N.; Hu, F.; Wang, Y. Y.; Niu, J. Y.; Wang, J. P. Double-malate bridging tri-lanthanoid cluster encapsulated arsenotungstates: syntheses, structures, luminescence and magnetic properties. *Dalton Trans.* **2015**, *44*, 11514−11523.

(29) Ma, P. T.; Hu, F.; Wan, R.; Huo, Y.; Zhang, D. D.; Niu, J. Y.; Wang, J. P. Magnetic double-tartaric bridging mono-lanthanide substituted phosphotungstates with photochromic and switchable luminescence properties. *J. Mater. Chem. C* **2016**, *4*, 5424−5433.

(30) Zheng, X.-Y.; Chen, M.-T.; Du, M.-H.; Wei, R.-J.; Kong, X.-J.; Long, L.-S.; Zheng, L.-S. Capturing lacunary iron−oxo Keggin clusters and insight into the Keggin-Fe$_{13}$ cluster rotational isomerization. *Chem. - Eur. J.* **2020**, *26*, 11985−11988.

(31) Li, S. R.; Wang, H. Y.; Su, H. F.; Chen, H. J.; Du, M. H.; Long, L. S.; Kong, X. J.; Zheng, L. S. A giant 3d-4f polyoxometalate super-tetrahedron with high proton conductivity. *Small Methods* **2020**, 2000777.

(32) Zheng, X. Y.; Du, M. H.; Amiri, M.; Nyman, M.; Liu, Q.; Liu, T.; Kong, X. J.; Long, L. S.; Zheng, L. S. Atomically precise lanthanide-iron-oxo clusters featuring the ε-Keggin ion. *Chem. - Eur. J.* **2020**, *26*, 1388−1395.

(33) Liu, J.-H.; Lin, L.-D.; Wang, G.-Q.; Li, L.-Y.; Sun, Y.-Q.; Li, X.-X.; Zheng, S.-T. All-inorganic open frameworks based on gigantic four-shell Ln@W$_8$@Ln$_8$@(SiW$_{12}$)$_6$ clusters. *Chem. Commun.* **2020**, *56*, 10305−10308.

(34) Li, H.-L.; Liu, Y.-J.; Liu, J.-L.; Chen, L.-J.; Zhao, J.-W.; Yang, G.-Y. Structural transformation from dimerization to tetramerization of serine-decorated rare-earth-incorporated arsenotungstates induced by the usage of rare-earth salts. *Chem. - Eur. J.* **2017**, *23*, 2673.

(35) Han, B.; Li, P. J.; Zhang, J.; Shi, H. Z. High color purity orange emitting KBaBP$_2$O$_8$:Eu^{3+} phosphor: synthesis, characterization and photoluminescence properties. *J. Lumin.* **2014**, *155*, 15−20.

(36) Huo, J. S.; Dong, L. P.; Lü, W.; Shao, B. Q.; You, H. P. Novel tunable green-red-emitting oxynitride phosphors co-activated with Ce^{3+}, Tb^{3+}, and Eu^{3+}: photoluminescence and energy transfer. *Phys. Chem. Chem. Phys.* **2017**, *19*, 17314−17323.

(37) Choi, Y. I.; Yoon, Y.; Kang, J.-G.; Sohn, Y. Photoluminescence imaging of Eu(III) and Tb(III)-embedded SiO$_2$ nanostructures. *J. Lumin.* **2015**, *158*, 27−31.

(38) Ito, T.; Yashiro, H.; Yamase, T. Regular Two-dimensional molecular array of photoluminescent Anderson-type polyoxometalate constructed by Langmuir−Blodgett technique. *Langmuir* **2006**, *22*, 2806−2810.

(39) Chen, L. J.; Zhang, F.; Ma, X.; Luo, J.; Zhao, J. W. Two types of novel tetra-iron substituted sandwich-type arsenotungastates with supporting lanthanide pendants. *Dalton Trans.* **2015**, *44*, 12598−12612.

(40) Yamase, T. Photo- and electrochromism of polyoxometalates and related materials. *Chem. Rev.* **1998**, *98*, 307−326.

(41) Zhao, J. W.; Luo, J.; Chen, L. J.; Yuan, J.; Li, H. Y.; Ma, P. T.; Wang, J. P.; Niu, J. Y. Novel 1-D double-chain organic−inorganic hybrid polyoxotungstates constructed from dimeric copper−lanthanide heterometallic silicotungstate units. *CrystEngComm* **2012**, *14*, 7981−7993.

(42) Ritchie, C.; Baslon, V.; Moore, E. G.; Reber, C.; Boskovic, C. Sensitization of lanthanoid luminescence by organic and inorganic ligands in lanthanoid-organic-polyoxometalates. *Inorg. Chem.* **2012**, *51*, 1142−1151.

(43) Lotfian, N.; Mirzaei, M.; Eshtiagh-Hosseini, H.; Löffler, M.; Korabik, M.; Salimi, A. Two supramolecular inorganic−organic hybrids of 12-silicotungstic acid heteropolyoxometalate and trinuclear lanthanide clusters: syntheses, structures, and magnetic properties. *Eur. J. Inorg. Chem.* **2014**, *2014*, 5908−5915.

(44) Aguilà, D.; Barrios, L. A.; Velasco, V.; Arnedo, L.; Aliagaalcalde, N.; Menelaou, M.; Teat, S. J.; Roubeau, O.; Luis, F.; Aromi, G. Lanthanide contraction within a series of asymmetric dinuclear [Ln$_2$] complexes. *Chem. - Eur. J.* **2013**, *19*, 5881−5891.

(45) Tan, X. F.; Zhou, J.; Fu, L. S.; Xiao, H. P.; Zou, H. H.; Tang, Q. L. A series of new lanthanide fumarates displaying three types of 3-D frameworks. *Dalton. Trans.* **2016**, *45*, 5253−5261.

(46) Nikiforov, V. N.; Koksharov, Y. A.; Gribanov, A. V.; Baran, M.; Irkhin, V. Y. Molecular magnetism and crystal field effects in the Kondo system Ce$_3$Pd$_{20}$(Si,Ge)$_6$ with two Ce sublattices. *J. Magn. Magn. Mater.* **2015**, *383*, 215−219.

(47) Sun, W.-B.; Han, B.-L.; Lin, P.-H.; Li, H.-F.; Chen, P.; Tian, Y.-M.; Murugesu, M.; Yan, P.-F. Series of dinuclear and tetranuclear lanthanide clusters encapsulated by salen-type and β-diketonate ligands: single-molecule magnet and fluorescence properties. *Dalton Trans.* **2013**, *42*, 13397−13403.

(48) Rogez, G.; Donnio, B.; Terazzi, E.; Gallani, J. L.; Kappler, J. P.; Bucher, J. P.; Drillon, M. The quest for nanoscale magnets: the example of [Mn$_{12}$] single molecule magnets. *Adv. Mater.* **2009**, *21*, 4323−4333.

(49) Kahn, M. L.; Sutter, J.; Golhen, S.; Guionneau, P.; Ouahab, L.; Kahn, O.; Chasseau, D. Systematic investigation of the nature of the coupling between a Ln(III) Ion (Ln = Ce(III) to Dy(III)) and its aminoxyl radical ligands. Structural and magnetic characteristics of a series of {Ln(organic radical)$_2$} compounds and the related {Ln(Nitrone)$_2$} derivatives. *J. Am. Chem. Soc.* **2000**, *122*, 3413−3421.

(50) Wu, M.; Jiang, F.; Kong, X.; Yuan, D.; Long, L.; Al-Thabaiti, S. A.; Hong, M. Two polymeric 36-metal pure lanthanide nanosized clusters. *Chem. Sci.* **2013**, *4*, 3104−3109.

(51) Gatteschi, D.; Sessoli, R. Quantum tunneling of magnetization and related phenomena in molecular materials. *Angew. Chem., Int. Ed.* **2003**, *42*, 268−297.

(52) Ren, M.; Bao, S. S.; Ferreira, R. A. S.; Zheng, L.-M.; Carlos, L. D. A layered erbium phosphonate in pseudo-D$_{5h}$ symmetry exhibiting field-tunable magnetic relaxation and optical correlation. *Chem. Commun.* **2014**, *50*, 7621−7624.

(53) Chen, L.; Zhou, J.; Yuan, A. H.; Song, Y. Slow magnetic relaxation in luminescent mononuclear dysprosium(III) and erbium-(III) pentanitrate complexes with the same LnO$_{10}$ coordination geometry. *Dalton Trans.* **2017**, *46*, 15812−15818.

(54) Woodruff, D. N.; Winpenny, R. E. P.; Layfield, R. A. Lanthanide Single-Molecule Magnets. *Chem. Rev.* **2013**, *113*, 5110−5148.

(55) Ma, P. T.; Hu, F.; Huo, Y.; Zhang, D. D.; Zhang, C.; Niu, J. Y.; Wang, J. P. Magnetoluminescent bifunctional dysprosium-based phosphotungstates with synthesis and correlations between structures and properties. *Cryst. Growth Des.* **2017**, *17*, 1947−1956.

(56) Kortz, U.; Muller, A.; van Slageren, J.; Schnack, J.; Dalal, N. S.; Dressel, M. Polyoxometalates: fascinating structures, unique magnetic properties. *Coord. Chem. Rev.* **2009**, *253*, 2315−2327.

(57) Ibrahim, M.; Mereacre, V.; Leblanc, N.; Wernsdorfer, W.; Anson, C. E.; Powell, A. K. Self-assembly of a giant tetrahedral 3d−4f single-molecule magnet within a polyoxometalate system. *Angew. Chem., Int. Ed.* **2015**, *54*, 15574−15578.